Supporting Information

Reductive Contact and Dipolar Interface Engineering Enable Stable Flexible $CsSnI_3$ Nanowire Photodetectors

Letian Dai[a,b,], Wanru Chen[c], Quanming Geng[a], Ying Xu[a], Guowu Zhou[d], Nuo Chen[e], Xiongjie Li[f,*]*

[a] Wuhan National Laboratory for Optoelectronics, Huazhong University of Science and Technology, 1037 Luoyu Road, Wuhan 430074, Hubei, P. R. China

[b] Optics Valley Laboratory, Hubei 430074, P. R. China

[c] Wuhan Huaming Renewable Energy Institute, 122 Zhongbei Road, Wuhan 430077, Hubei, P.R. China

[d] Wuhan Haisipulin Technology Development Co., Ltd, 897 Gexin Road, Wuhan, 430023, Hubei, P.R. China

[e] Department of Electrical Engineering, Karlsruhe Institute of Technology, Karlsruhe 76131, Germany

[f] Key Laboratory of Catalysis and Energy Materials Chemistry of Ministry of Education & Hubei Key Laboratory of Catalysis and Materials Science, Key Laboratory of Analytical Chemistry of the State Ethnic Affairs Commission, Hubei R&D Center of Hyperbranched Polymers Synthesis and Applications, South-Central Minzu University, Wuhan, Hubei, 430074, P.R. China

*Email: ldai@hust.edu.cn, xiongjieli@mail.scuec.edu.cn.

S1. Materials and Preparation

CsI (99.99%, Alfa Aesar), SnI_2 (99.99%, Sigma-Aldrich), DMF (*N*,*N*-dimethylformamide, 99.8%, Sigma-Aldrich), DMSO (Dimethyl sulfoxide, 99.5%, Sigma-Aldrich), PMMA (Poly(methyl methacrylate), average Mw ~15,000 by GPC, Macklin), Cabon rod (100mm, diameter 5.0mm, Macklin) and 3F-2NA (3-Fluoro-2-nitroanisole, 99.7%, Macklin) were used as received without further purification. Aluminum foil (type 1060) with a thickness of 0.2 mm and a high purity ≥ 99.60% was obtained from an enterprise in Hubei province of China. A 200 mL aqueous solution of 18 wt% sulfuric acid was prepared by slowly adding 22 mL of concentrated H_2SO_4 (98%, Macklin) into 178 mL of deionized water under constant stirring and cooling.

S2. Fabrication of $CsSnI_3$ Nanowire Photodetector

Prior to use, the aluminum foil was ultrasonically cleaned in ethanol for 15 min and dried under nitrogen. Anodization was performed in 18 wt% H_2SO_4 at 0–5 °C under 25 V for 60 min to form an anodic Al_2O_3 layer. After rinsing and drying, a nanosecond 650 nm pulsed laser was used to locally ablate the Al_2O_3 layer, exposing the metallic Al regions that act as the conductive base.

The effective area of the device was defined by the laser-patterned circular opening on the anodized Al_2O_3/Al substrate, where metallic Al was exposed and $CsSnI_3$ nanowires were selectively grown. The diameter of the circular active region was approximately 3 mm, corresponding to a geometric area of ~0.071 cm². This value is consistent with the illumination area of ~0.07 cm² used in the optoelectronic measurements, ensuring that the measured photocurrent originates from the predefined active nanowire device region.

In a glovebox environment with O_2 and H_2O levels maintained below 0.01 ppm, a 1.5 M $CsSnI_3$ precursor solution (prepared by dissolving CsI and SnI_2 in a stoichiometric ratio of 1:1 in DMF) was drop-cast onto the laser-exposed Al surface and dried at room temperature for 12 h under a controlled solvent evaporation rate of ~1 μL h^{-1}. During this slow-drying process, yellow δ-$CsSnI_3$ nanowires spontaneously formed. The resulting nanowire film was subsequently annealed at 160 °C for 20 min, leading to the formation of the black γ-$CsSnI_3$ phase. After phase transformation, a 5 wt% 3F-2NA

solution in chlorobenzene was spin-coated onto the nanowire array at 3000 rpm for 30 s, followed by a mild post-annealing step at 80 °C for 10 min to form a stable interfacial dipole layer.

Subsequently, a compact NiO_x layer (20 nm) serving as the hole transport layer (HTL), followed by a 250 nm ITO top transparent electrode, were sequentially deposited onto the $CsSnI_3$ nanowires by sputtering.

Finally, the device was encapsulated with a thin PMMA layer to prevent the oxidation of Sn^{2+} species.

S3. Characterization Techniques

XRD measurements were carried out using a PANalytical X'Pert PRO diffractometer (Cu Kα, λ = 1.5406 Å). XPS and UPS spectra were collected using a Shimadzu AXIS-ULTRA DLD-600 W system. Surface morphology was examined using a Nova Nano SEM 450. UV–Vis absorption spectra were recorded using a Lambda 950 spectrophotometer, while steady-state PL and TRPL spectra were measured using an Edinburgh FLS 980 system with a 405 nm excitation source.

The optoelectronic properties of the flexible $CsSnI_3$ nanowire photodetector were evaluated at room temperature under 850 nm laser illumination. A focused beam (~3 mm diameter) illuminated the active area (0.071 cm^2), with the power density adjustable from 1.33×10^{-5} to 8.39×10^2 $mW \cdot cm^{-2}$. Photoresponse curves were recorded with a Keithley 2400 source meter. Under a 0.1 V bias and 850 nm illumination, the power-dependent photocurrent, linear dynamic range, ON/OFF ratio, and temporal response were measured. The photocurrent shows linear dependence over the range of 1.33×10^{-5}–8.39×10^2 $mW \cdot cm^{-2}$.

For the environmental storage test, the PMMA-encapsulated devices were stored under ambient laboratory conditions at approximately 20 °C and 40–60% relative humidity, and the photocurrent retention was periodically measured over 60 days. For the mechanical durability test, the devices were subjected to repeated bending at a fixed bending radius of 5 mm for up to 1000 cycles, and the photocurrent was recorded after selected bending intervals.

S4. Time-Resolved Photoluminescence (TRPL) Analysis

The time-resolved photoluminescence (TRPL) decay curves of $CsSnI_3$ nanowire films were fitted using a bi-exponential function, as shown in Equation (S1):

$$I(t) = A_1 e^{-\frac{t}{\tau_1}} + A_2 e^{-\frac{t}{\tau_2}} + I_0 \quad \text{(S1)}$$

where A_1 and A_2 are the relative amplitudes, $\tau_1$and τ_2 are the fast and slow decay lifetimes, and I_0 is a baseline offset.

The average carrier lifetime $\tau_{average}$ was calculated using Equation (S2):

$$\tau_{average} = \frac{A_1\tau_1^2 + A_2\tau_2^2}{A_1\tau_1 + A_2\tau_2} \quad \text{(S2)}$$

The fitted parameters (A_1, A_2,τ_1, τ_2) were obtained from the bi-exponential fitting of Figure S14.

Note S1. Calculation of EQE, NEP, and specific detectivity

The external quantum efficiency (EQE) of the photodetector was calculated from the measured responsivity according to：

$$EQE = \frac{Rhc}{q\lambda}$$

where R is the responsivity, h is Planck's constant, c is the speed of light, q is the elementary charge, and λ is the incident wavelength. When R is expressed in A W^{-1} and λ in nm, the equation can be written as:

$$EQE = \frac{1240R}{\lambda} \times 100\%$$

For the $CsSnI_3$ nanowire photodetector in this work, R=0.39 A W^{-1} at 850 nm, giving an EQE of approximately 56.9%.

To evaluate the noise characteristics of the $CsSnI_3$ nanowire photodetector, the frequency-resolved current noise spectral density was measured under dark conditions at a bias of 0.1 V. The noise-current spectral density i_n is expressed in units of A $Hz^{-1/2}$. The corresponding noise-equivalent power (NEP) can be calculated as:

$$NEP = \frac{i_n}{R}$$

where R is the responsivity of the photodetector. Using the measured white-noise floor of approximately 7.5×10^{-15} A $Hz^{-1/2}$ and R=0.39 A W^{-1} at 850 nm, the NEP is estimated to be approximately 1.9×10^{-14} W $Hz^{-1/2}$. The specific detectivity based on the measured noise-current spectral density is then calculated as:

$$D^* = \frac{\sqrt{S}}{NEP} = \frac{R\sqrt{S}}{i_n}$$

where S is the effective device area. In comparison, the shot-noise-limited noise current is estimated by:

$$i_{shot} = \sqrt{2qI_{dark}}$$

where q is the elementary charge and I_{dark} is the dark current. The corresponding shot-noise-limited detectivity is:

$$D^{*}_{shot} = \frac{R\sqrt{S}}{\sqrt{2qI_{dark}}}$$

In the present device, the measured noise spectrum exhibits a low-frequency 1/f-noise region and a high-frequency white-noise-limited region. The detectivity reported in the main text was evaluated using the measured noise-current spectral density in the white-noise-limited regime. This measured-noise-based analysis avoids relying solely on the ideal shot-noise-limited assumption and provides a more rigorous validation of the low-noise operation of the $CsSnI_3$ nanowire photodetector.

In Table S3, "measured-noise-based" indicates that NEP or D^* was calculated from the measured current-noise spectral density; "shot-noise-estimated" indicates that the noise was estimated from the dark-current shot-noise expression; and "D^*-derived" indicates that NEP was back-calculated from a reported D^* value when NEP was not directly reported.

Note S2. Bending strain estimation and mechanical fatigue analysis

The bending strain during repeated mechanical deformation was estimated using the standard relation:

$$\varepsilon = \frac{t}{2R}$$

where t is the thickness of the mechanically dominant flexible substrate and R is the bending radius. In this work, the Al substrate thickness is approximately 0.2 mm and the bending radius was fixed at 5 mm. Therefore, the maximum surface strain is estimated to be:

$$\varepsilon = \frac{0.2\ mm}{2 \times 5\ mm} \approx 0.02 = 2\%$$

The flexible Al substrate accommodates a significant fraction of the applied strain because of its ductility. In addition, the vertically aligned $CsSnI_3$ nanowire architecture helps distribute the local strain and suppress long-range crack propagation compared with continuous thin films. After deposition of NiO_x and ITO, the nanowires form a composite coated structure, which may reduce local mechanical compliance. Therefore, repeated bending can induce localized nanowire fracture or coating discontinuity. However, the overall nanowire network remains largely continuous after bending, preserving sufficient electrical pathways and enabling the device to retain ~94% of its initial photocurrent after 1000 bending cycles.

Note S3. DFT calculation details and dipole-moment analysis

All adsorption-configuration optimizations of 3F-2NA on the $CsSnI_3$ (202) surface were performed using the CASTEP module in Materials Studio. The generalized gradient approximation (GGA) with the Perdew–Burke–Ernzerhof (PBE) exchange-correlation functional was employed, together with ultrasoft pseudopotentials. A plane-wave cutoff energy of 571.4 eV was used. The $CsSnI_3$ (202) surface was modeled using a periodic slab, and a vacuum layer larger than 15 Å was introduced along the surface-normal direction to avoid artificial interactions between adjacent slabs. A Monkhorst–Pack k-point grid of 2 × 2 × 1 was used for the surface calculations. The convergence criteria were set to 2.0×10^{-7} eV atom^{-1} for total energy, 2.4×10^{-3} eV Å^{-1} for maximum force, and 1.4×10^{-3} Å for maximum atomic displacement.

To further evaluate the intrinsic molecular polarity of 3F-2NA, an additional dipole-moment calculation was carried out using the DMol³ module at the GGA-PBE level with a DNP basis set and all-electron treatment. The calculated molecular dipole moment is 6.11 Debye, with dipole-vector components of 0.844, 2.224, and 0.336 a.u. along the x, y, and z directions, respectively. The dipole vector is mainly dominated by the y-component, indicating pronounced anisotropic charge distribution within the molecule. The exact absolute value of the dipole moment may vary slightly depending on the computational implementation and basis description; nevertheless, both calculations consistently indicate that 3F-2NA possesses a relatively large intrinsic dipole. Different adsorption configurations mainly alter the orientation of this intrinsic dipole relative to the $CsSnI_3$ surface, thereby leading to distinct interfacial dipole-alignment tendencies.

Note S4. Space-charge-limited current measurements of carrier-only $CsSnI_3$ nanowire devices

To evaluate the trap density and carrier mobility of the $CsSnI_3$ nanowires, SCLC measurements were carried out using electron-only and hole-only devices. The trap density was estimated from the trap-filled-limit voltage according to:

$$N_t = \frac{2\varepsilon_0\varepsilon_r V_{TFL}}{qL^2}$$

where N_t is the trap density, ε_0 is the vacuum permittivity, ε_r is the relative dielectric constant of $CsSnI_3$, V_{TFL} is the trap-filled-limit voltage, q is the elementary charge, and L is the effective transport length.

The carrier mobility was extracted from the SCLC Child regime using:

$$J = \frac{9\varepsilon_0\varepsilon_r\mu V^2}{8L^3}$$

For nanowire-based carrier-only devices, the equation can also be expressed using the current along the nanowire:

$$I = JA$$

and therefore:

$$\mu = \frac{8LI}{9\varepsilon_0\varepsilon_r V^2}$$

where I is the current along the nanowire, V is the applied voltage, and L is the effective nanowire transport length. In this work, ε_0=8.8542×10^{-12} C V^{-1} m^{-1} and ε_r=29 were used for $CsSnI_3$. Based on the Child-regime fitting of the carrier-only SCLC curves, the electron and hole mobilities of the $CsSnI_3$ nanowires were estimated to be 762 and 692 cm^2 V^{-1} s^{-1}, respectively. These values should be regarded as effective mobilities of the $CsSnI_3$ nanowires under the carrier-only measurement geometry.

S5. Supplementary Figures and Tables

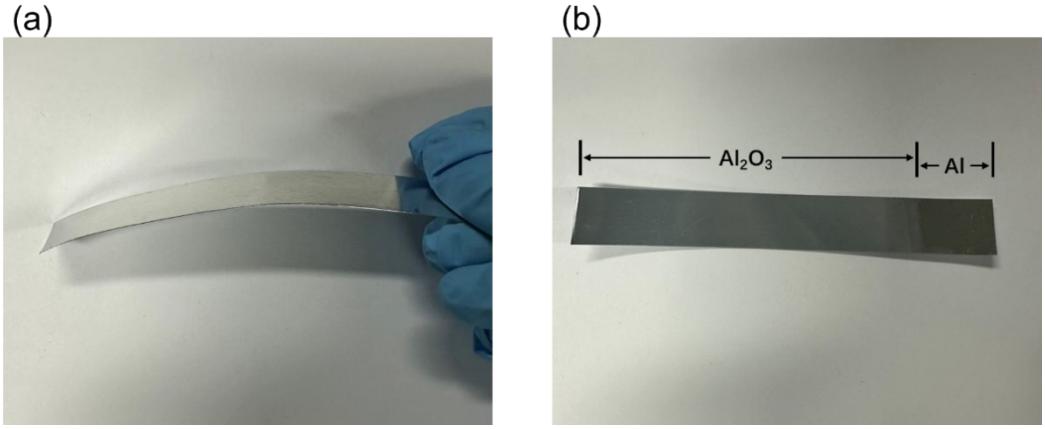

Figure S1. Photographs of 0.2 mm-thick 1060 aluminum foil before and after anodization. (a) Pristine smooth and flexible foil; (b) surface covered by a gray-white Al_2O_3 layer after anodization.

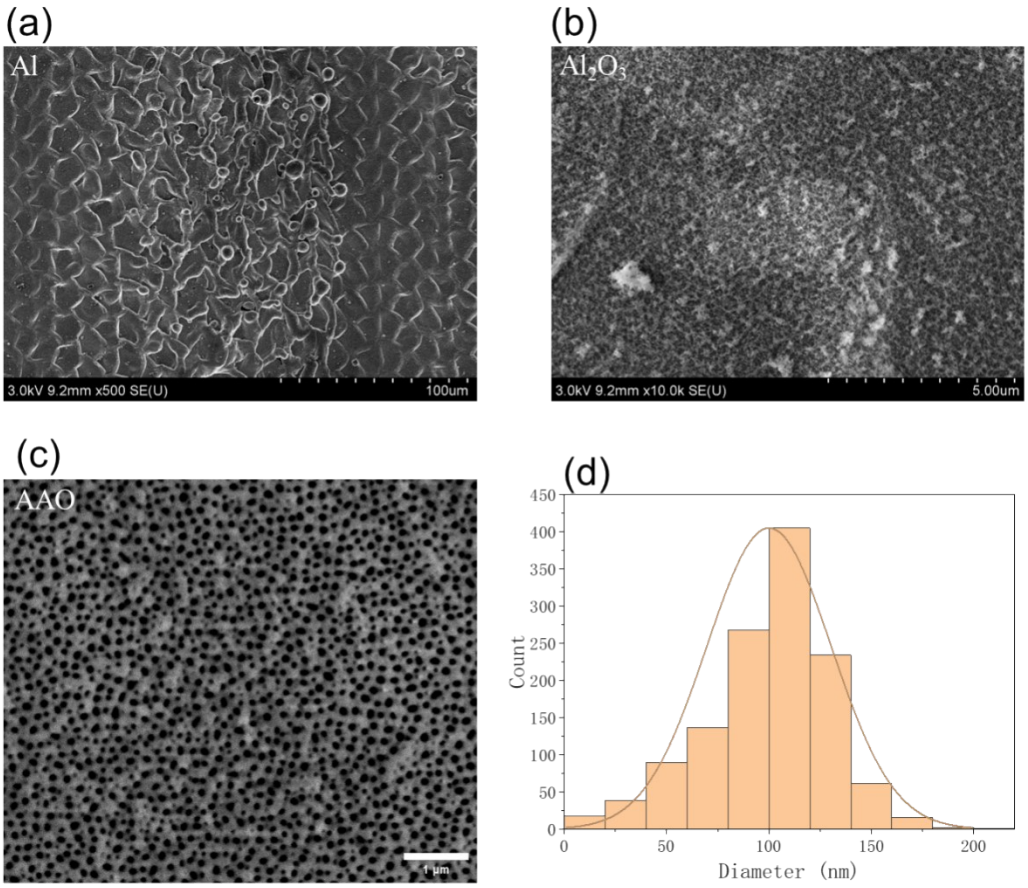

Figure S2. Surface morphology of aluminum foil before and after anodization. (a, b) scanning electron microscopy (SEM) images of pristine and anodized Al foil; (c) Top-view SEM image of anodic aluminum oxide (AAO) layer with ~100 nm pores (Scale bar: 1 μm); (d) Corresponding pore size distribution extracted from the SEM image in (c).

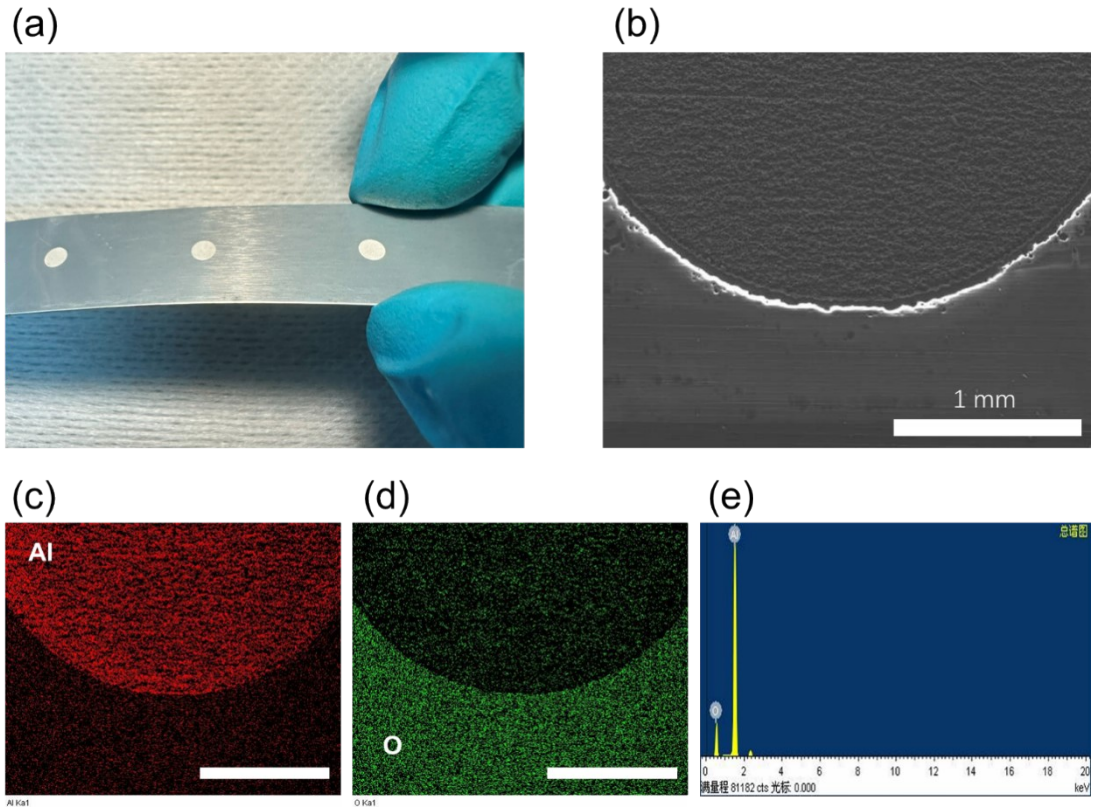

Figure S3. (a) Photograph of circular laser-ablation windows on the anodized Al foil; (b) SEM image of a localized laser-ablated region, showing the clear boundary between the exposed metallic Al and the remaining Al_2O_3 layer (scale bar: 1 mm); (c, d) EDX elemental maps of Al and O, respectively (scale bars: 1 mm); (e) Corresponding EDX spectrum of anodized Al foil.

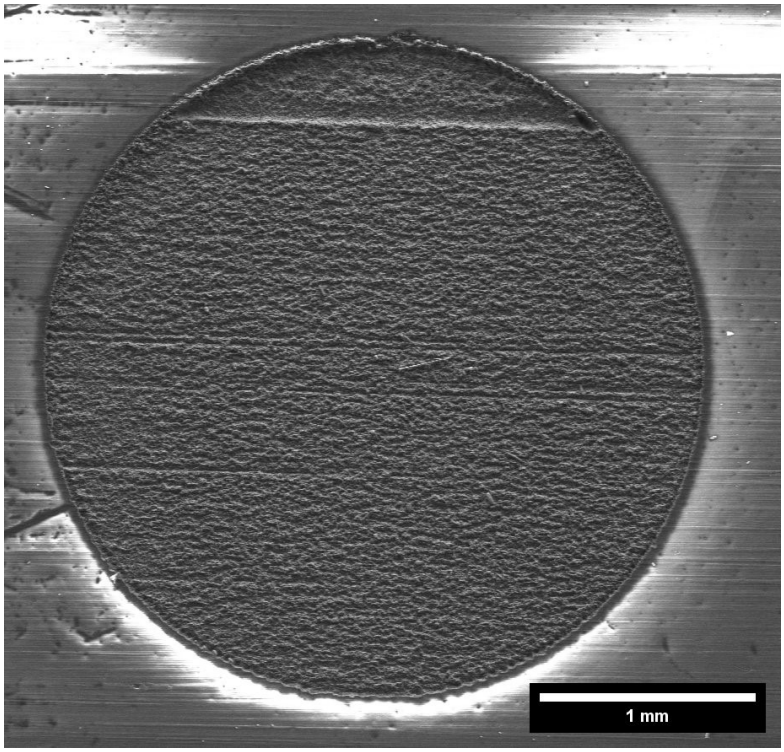

Figure S4. Scanning electron microscopy (SEM) image of the laser-patterned circular opening on the anodized Al_2O_3/Al substrate. The diameter of the opening is approximately 3 mm, corresponding to a geometric area of ~0.071 cm^2. This region serves as the predefined active area for subsequent nanowire growth and device fabrication. Scale bar: 1 mm.

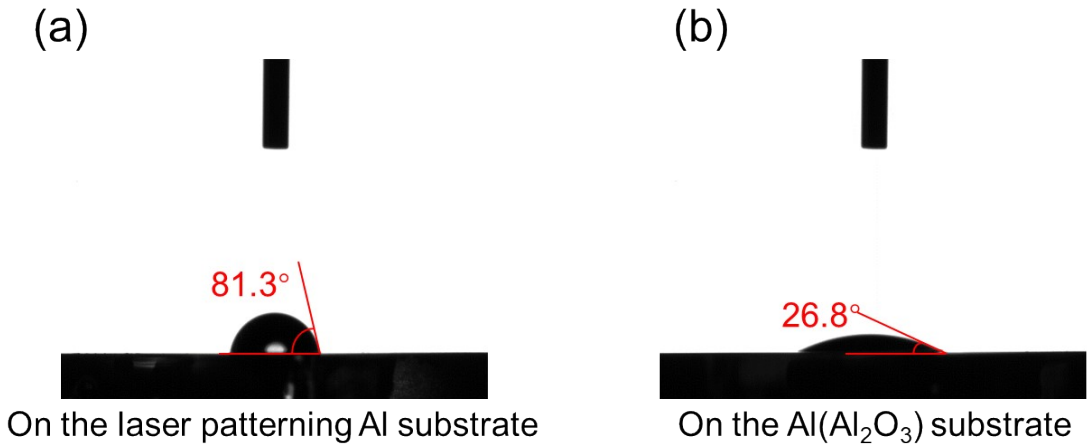

Figure S5. Contact-angle measurements of $CsSnI_3$ precursor solution. (a) On laser-ablated Al surface (81.3°); (b) On anodized Al_2O_3 surface (26.8°).

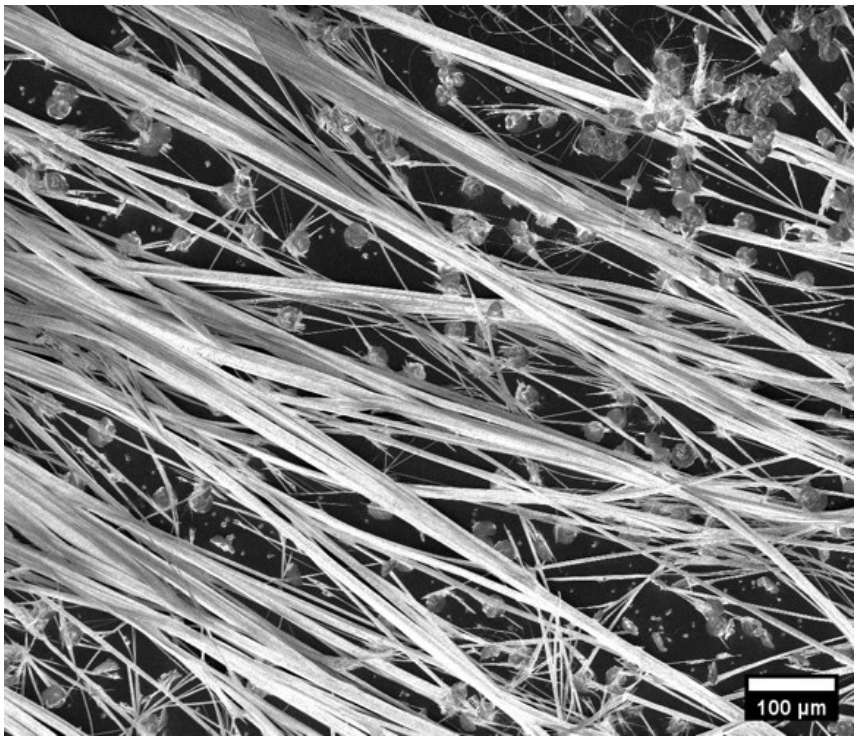

Figure S6. SEM image showing the lateral growth morphology of $CsSnI_3$ microwires formed on the anodized Al_2O_3 surface (scale bar: 100 µm).

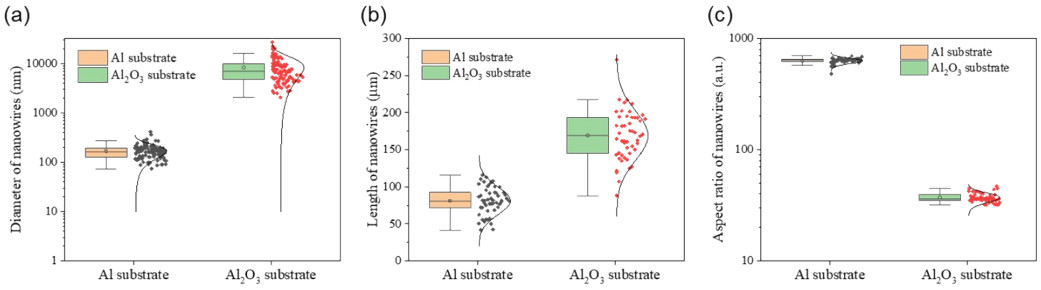

Figure S7. Statistical analysis of $CsSnI_3$ nanostructures grown on metallic Al and Al_2O_3 substrates. (a) Diameter distributions of $CsSnI_3$ nanowires on metallic Al and microrods/microwires on Al_2O_3. (b) Length distributions of $CsSnI_3$ nanostructures grown on metallic Al and Al_2O_3. (c) Corresponding aspect-ratio distributions.

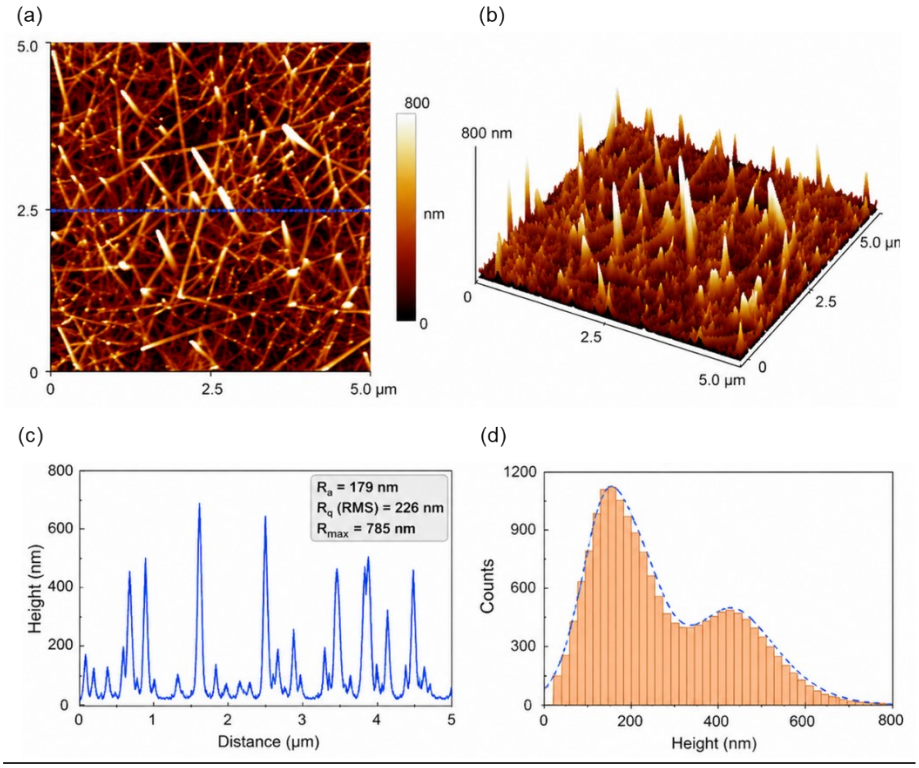

Figure S8. AFM characterization of the $CsSnI_3$ nanowire network grown on metallic Al. (a) 2D AFM height image measured over a 5 µm × 5 µm area. (b) Corresponding 3D AFM topography. (c) Representative line-scan profile along the marked region. The extracted root-mean-square roughness (R_q) is ~226 nm, and the peak-to-valley height is ~785 nm. (d) Height distribution histogram extracted from the AFM height image.

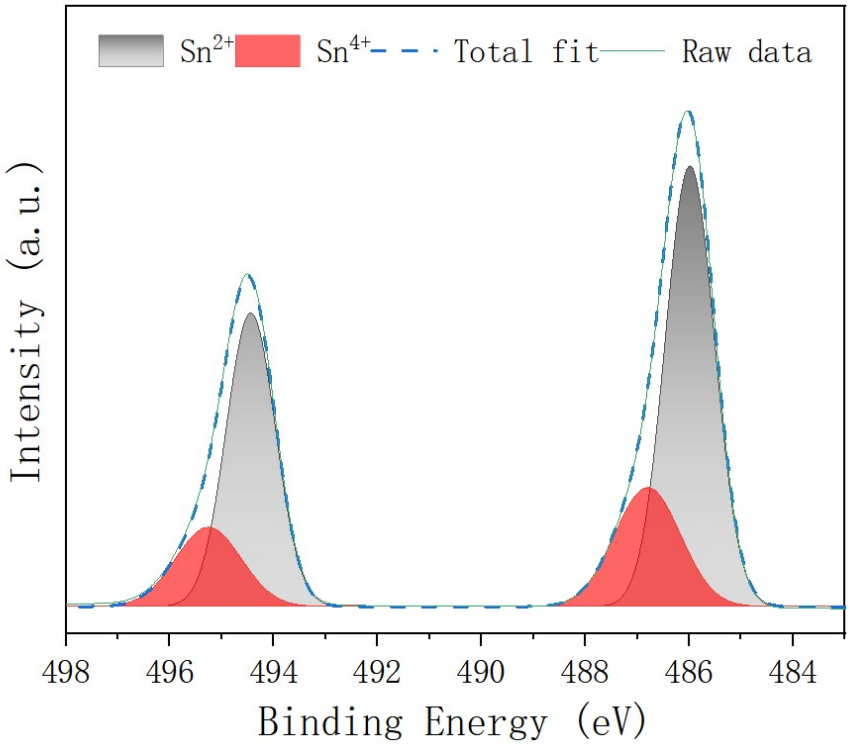

Figure S9. Sn 3d XPS of $CsSnI_3$ films grown on inert glass substrates under otherwise identical conditions. The fitted Sn^{2+}/Sn^{4+} ratio is 73.4%/26.6%, close to that of the Al_2O_3-supported sample and much lower than that of the metallic-Al-supported sample, supporting the substrate-dependent reductive effect of metallic Al.

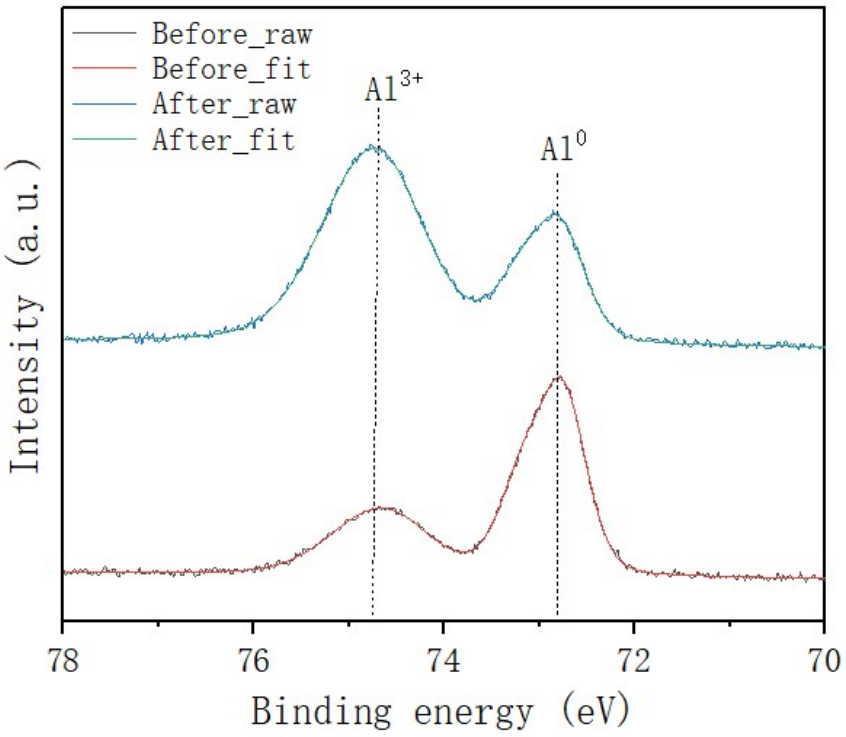

Figure S10. Al 2p XPS spectra of the laser-exposed Al surface before and after $CsSnI_3$ growth.

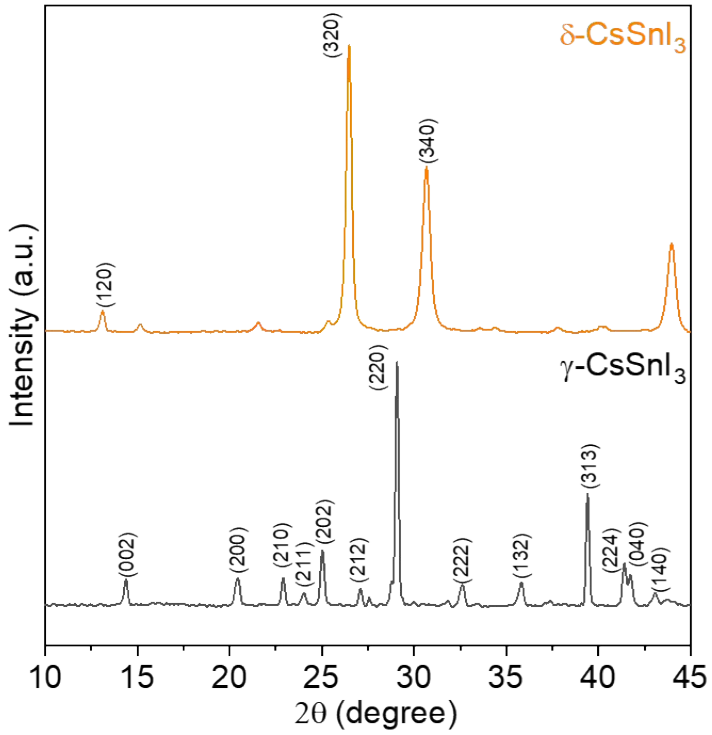

Figure S11. X-ray diffraction (XRD) patterns of $CsSnI_3$ showing the yellow δ-phase before annealing and the black γ-phase after annealing at 160 °C.

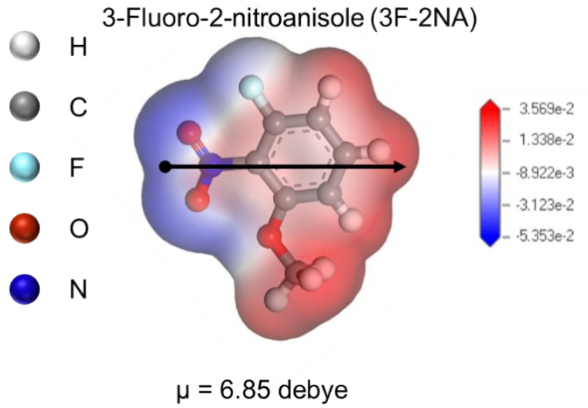

Figure S12. Molecular electrostatic potential (MEP) map of 3F-2NA.

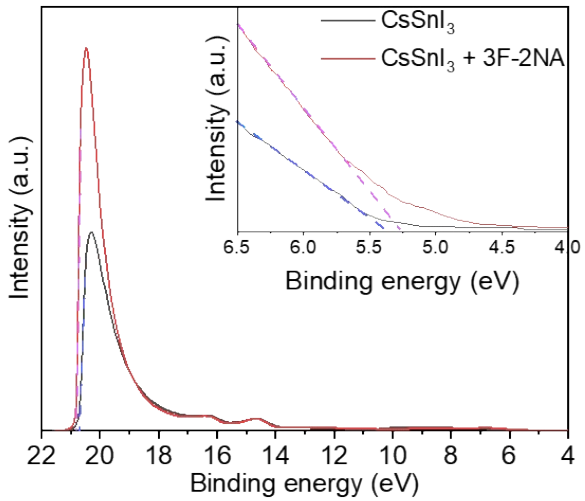

Figure S13. Ultraviolet photoelectron spectroscopy (UPS) spectra of pristine and 3F-2NA-modified $CsSnI_3$ films.

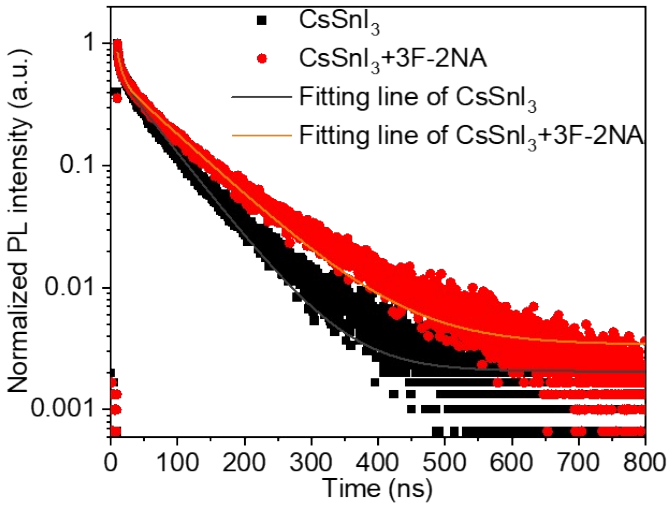

Figure S14. TRPL decay curves of $CsSnI_3$ nanowires with and without 3F-2NA modification, with bi-exponential fitting.

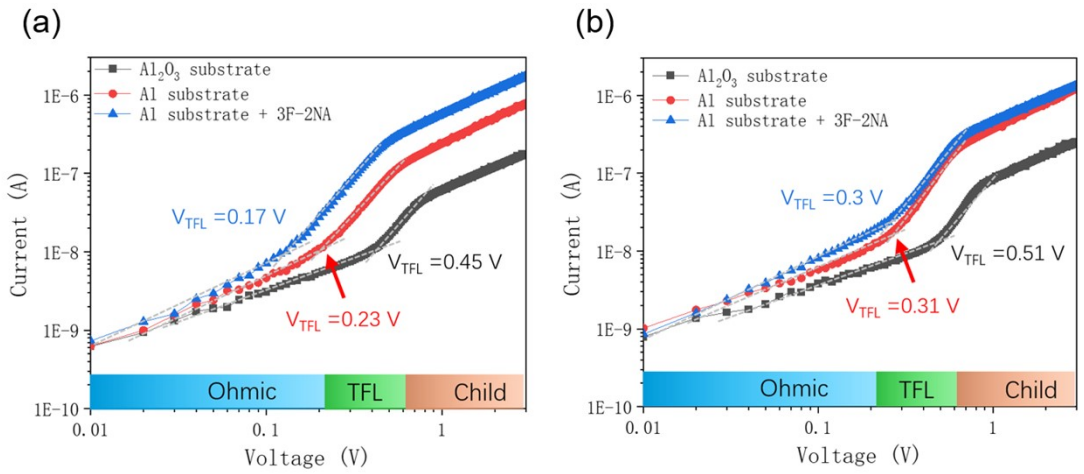

Figure S15. SCLC characterization of carrier-only $CsSnI_3$ nanowire devices.

(a) Current–voltage curves of electron-only devices fabricated on Al_2O_3 substrate, Al substrate, and Al substrate with 3F-2NA modification. (b) Current–voltage curves of the corresponding hole-only devices.

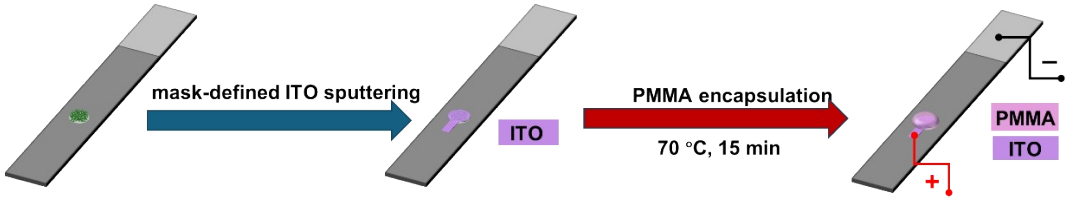

Figure S16. Shadow-mask-assisted deposition of ITO followed by PMMA encapsulation.

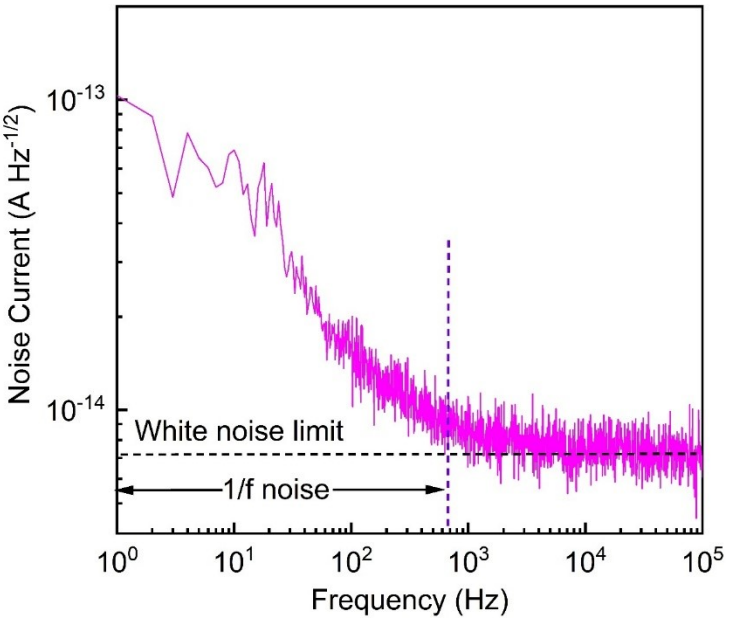

Figure S17. Noise-current spectral density of the $CsSnI_3$ nanowire photodetector. Frequency-resolved current noise spectral density measured under dark conditions at a bias of 0.1 V. The spectrum shows a low-frequency 1/f-noise region and a high-frequency white-noise-limited regime, with a white-noise floor of approximately 7.5×10^{-15} A $Hz^{-1/2}$.

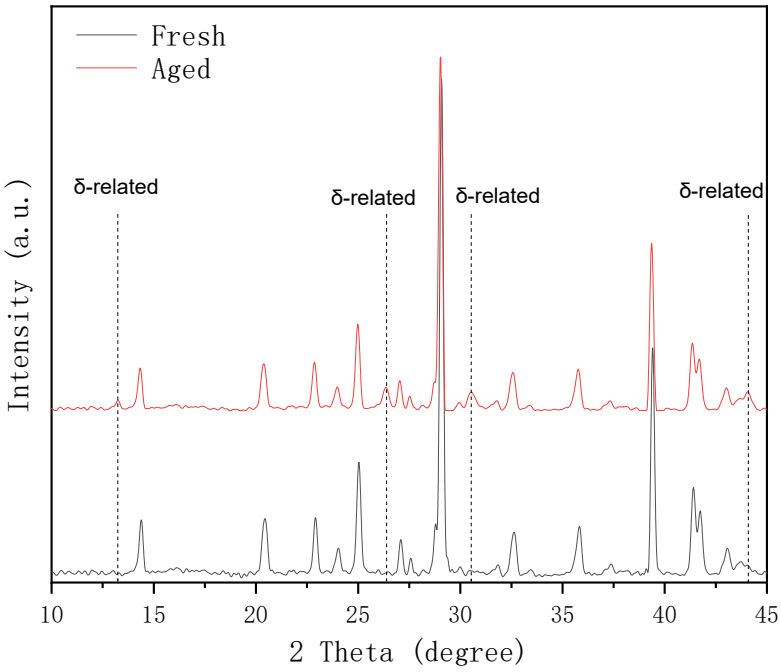

Figure S18. XRD comparison of fresh and aged $CsSnI_3$ nanowire films. The aged sample was stored under ambient laboratory conditions for 60 days.

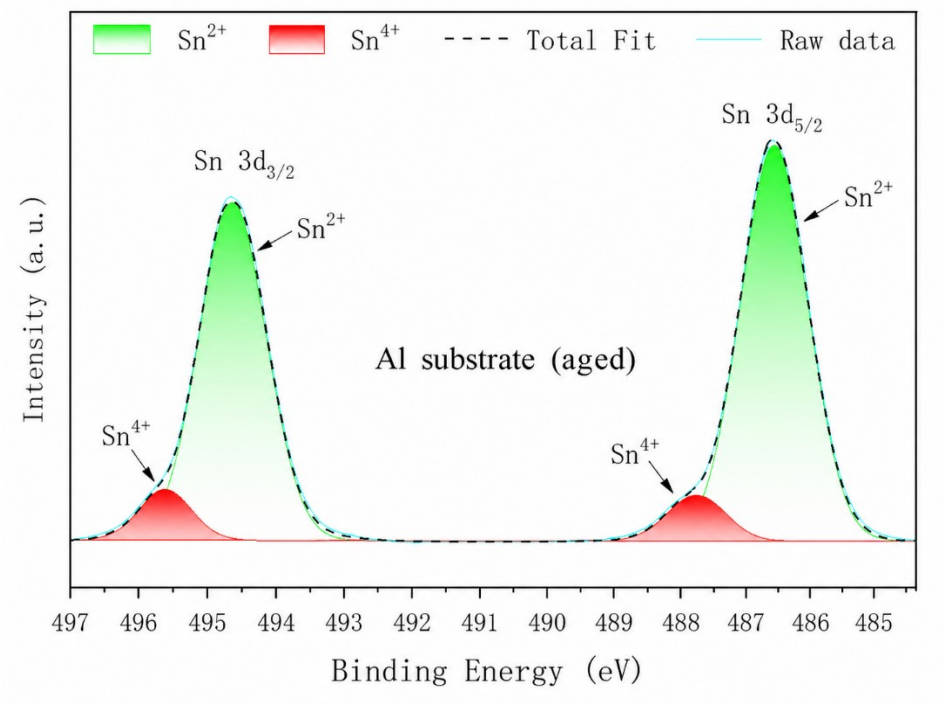

Figure S19. Sn 3d XPS of aged $CsSnI_3$ nanowire films.

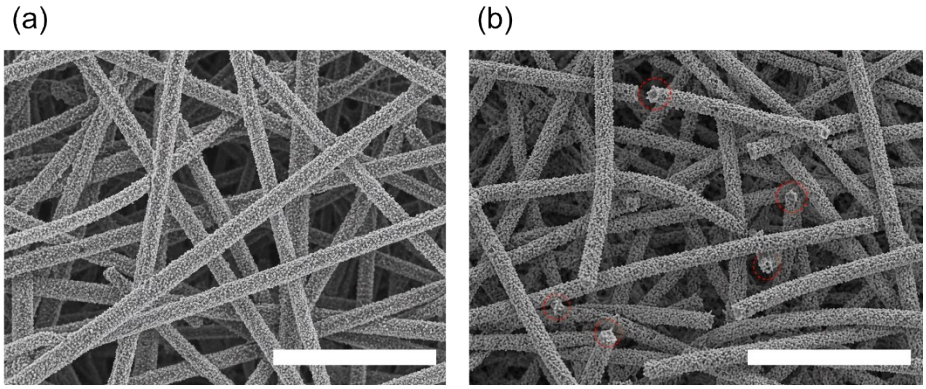

Figure S20. SEM images of ITO-coated $CsSnI_3$ nanowires before and after bending. (a) ITO-coated $CsSnI_3$ nanowire network before bending. (b) ITO-coated $CsSnI_3$ nanowire network after 1000 bending cycles, where localized defects and partial nanowire discontinuities are marked by red circles. Scale bars: 1 μm.

Table S1. Bi-exponential TRPL fitting parameters for pristine and 3F-2NA-modified $CsSnI_3$.

	A_1	τ_1 (ns)	A_2	τ_2 (ns)	y_0	t_{avg} (ns)
$CsSnI_3$	0.331	6.334	0.537	61.963	0.002	58.67
$CsSnI_3$ + 3F-2NA	0.343	6.714	0.503	86.487	0.003	82.47

Table S2. Trap-density comparison of $CsSnI_3$ nanowires grown on different substrates and with interfacial modification.

Sample	Electron trap density (cm^{-3})	Hole trap density (cm^{-3})
$CsSnI_3$ NWs on Al_2O_3	5.77×10^{11}	6.54×10^{11}
$CsSnI_3$ NWs on Al	2.95×10^{11}	3.97×10^{11}
$CsSnI_3$ NWs on Al with 3F-2NA	2.05×10^{11}	3.85×10^{11}

Table S3. Benchmarking of the $CsSnI_3$ nanowire photodetector against representative Pb-free NIR photodete

EQE and NEP valu

responsivity, waveleng

quantum dots, NS is na

Category	Material / Device	Pb-free	Flexible	Wavelength (nm)	Responsivity (mA W⁻¹)	EQE (%)	D* (Jones)	NEP (W Hz⁻¹/²)	Noise / NEP basis	Response time	LDR (dB)	Bias (V)	Operational lifetime / durability	Reference
Lead-free Sn-based	$CsSnI_3$ NW array	Yes	Yes	850	390	56.9% at 850 nm	1.38×10^{13}	1.9×10^{-14}	measured-noise-based; from white-noise floor and R	30/30 ms	156	0.1	98% after 6000 s continuous ON/OFF operation; 85% after 60 d ambient storage; 94% after 1000 bending cycles	This work
Lead-free Sn-based	$CsSnI_3$ NW array	Yes	No	940	54	7.1% at 940 nm	3.85×10^{5}	~2.6×10^{-11}	shot-noise-estimated / D*-derived	83.8/243.4 ms	–	0.1	Repeatable 940 nm photoresponse; PMMA-protected optical stability up to 6 d	[1]
Lead-free Sn-based	$CsSnI_3$ NW array	Yes	No	405	237	72.6% at 405 nm	1.18×10^{12}	~1.7×10^{-12}	estimated from reported noise	0.23/0.19 ms	180	0	No degradation after >1200 s continuous illumination; >90% after 60 d storage	[2]
Lead-free Sn-based	$FASnI_3$-CNI TF	Yes	Yes	785	370	63.2% at 785 nm	9.12×10^{12}	2.1×10^{-13}	measured-noise-based at 100 Hz	4.17/3.91 µs	–	0	Wearable heart-rate monitoring under 200 µW cm⁻² at 0 V	[3]
Lead-free Sn-based	$FASnI_3$-BDADI TF	Yes	No	808	5900	apparent EQE ≈ 906% at 808 nm; reported 60–80% over 400–900 nm	1.06×10^{14}	~1.9×10^{-15}	shot-noise-estimated	14.1/25.3 µs	96.44	0	~80% R retained after 50 d in N glovebox; ~80% photocurrent retained after continuous operation	[4]
Lead-free Sn-based	$CsSnBr_3$ QDs	Yes	Yes	410	62.3	~18.8% at 410 nm	4.27×10^{11}	~9.1×10^{-13}	shot-noise-estimated; not directly reported	50/51 ms	–	3	>80% photocurrent retained after 100 bending cycles	[5]
Lead-free Bi-based	$MA_3Bi_2I_9$ TF	Yes	No	382	280	90.9% at 382 nm, 0 V	8.8×10^{12}	~5.7×10^{-14}	D*-derived	0.38/0.45 s	–	0	Non-encapsulated devices stored in air (RH ≥75%, dark, room temperature) retained response over long-term storage	[6]
Lead-free Bi-based	$MA_3Bi_2I_6Cl_3$ TF	Yes	Yes	382	920	~302% at 382 nm	2.9×10^{13}	~1.7×10^{-14}	D*-derived / shot-noise-estimated	0.46/0.41 s	–	0	Flexible device retained ~85% initial photoresponse after 5000 bending cycles	[7]
Lead-free Bi-based	$Cs_3Bi_2I_9$ TF	Yes	No	365	1570	~509% at 365 nm	3.38×10^{13}	~1.5×10^{-14}	D*-derived / shot-noise-estimated	0.45/0.50 s	–	0	Ambient air, RH >50%, room temperature; ~98% response retained after 100 d	[8]
Representative Pb-based	CsPbI NW array	No	No	Halogen light	6.7	~15–17% peak at ~430–500 nm, 1 V bias	1.57×10^{9}	~1.1×10^{-9}	D*-derived; not directly reported	292/234 ms	–	5	Stable cubic phase at room temperature; stable in IPA after 30 d	[9]
Representative Pb-based	$CsPbBr_3$ NS	No	Yes	517	640	~154% at 517 nm	–	6.6×10^{-14}	reported NEP	19/25 µs	–	10	<2.6% fluctuation after 12 h illumination; >10000 bending cycles with <3% fluctuation	[10]
Representative Pb/Sn-based	$CsPb_xSn_{1-x}(Br_yI_{1-y})_3$ alloy NWs	No	No	473	8.5	~2.2% at 473 nm	2×10^{10}	~$5.5–5.9 \times 10^{-12}$	shot-noise-estimated	4.25/4.82 ms	120	1	Only ~10% photocurrent degradation after 30 min irradiation	[11]
Representative Pb-based	$MAPbI_3$ NW array	No	Yes	473	560	~147% at 473 nm	4.16×10^{12}	~3.6×10^{-14}	shot-noise-estimated	0.2/0.37 ms	89	5	>80% performance retained after 30 d in air (55–65% RH); stable after bending	[12]
Representative Pb-based	$MAPbI_3$ NW array	No	Yes	532	227	~52.9% at 532 nm	1.36×10^{11}	~6.5×10^{-13}	D*-derived using 1 mm spot area	61/42 ms	–	0	~7.9% photocurrent decrease after 1500 bending cycles at ~75°	[13]
Representative Pb-based	$CsPbBr_3$ TF	No	No	405	965	~295% at 405 nm	3.39×10^{10}	1.9×10^{-15}	D*-derived	20.51/30 ms	–	0	Vertical self-powered device retained ~70% photocurrent after 120 d air exposure	[14]
Representative Pb-based	$MAPbI_{3-x}Br_x$ TF	No	No	632	45000	8.84×10^{4}% at 632 nm	1.15×10^{14}	2.75×10^{-15}	reported / measured-noise-based	0.24/0.38 s	–	0	Non-encapsulated device: ~29% R loss after 500 h under simulated sunlight	[15]

Table S4. Summary of the individual contributions of Al reductive contact, 3F-2NA dipolar interlayer, and PMMA encapsulation to device stability.

Stabilization component	Main function	Supporting evidence	Stability contribution
Metallic Al interface	Growth-stage redox control	Higher Sn^{2+} fraction in $CsSnI_3$ grown on metallic Al than on Al_2O_3/glass	Suppresses Sn^{4+} accumulation during nanowire crystallization
3F-2NA dipolar layer	Interfacial electronic stabilization	UPS-derived barrier reduction and TRPL lifetime increase	Improves charge extraction and reduces interfacial recombination
PMMA encapsulation	External environmental protection	Encapsulated/unencapsulated comparison under 850 nm cycling	Blocks moisture/oxygen-induced degradation
Complete device	Hierarchical stabilization	6000 s operational stability, 60-day ambient storage, and 1000 bending cycles	Combines growth-stage chemical stabilization, interface stabilization, and environmental protection

Table S5. Pixel-to-pixel reproducibility and working-pixel yield of the 4 × 4 $CsSnI_3$ nanowire photodetector array. The photocurrent was measured under 850 nm illumination at 2.5×10^2 mW cm^{-2} and 0.1 V bias, while the dark current was measured under complete dark conditions at 0.1 V bias.

Pixel No.	Device ID	Dark current (A)	Photocurrent under 850 nm (A)	Normalized photocurrent (%)
1	Pixel 1	3.47E-10	8.36E-05	88.00
2	Pixel 2	3.77E-10	8.74E-05	92.00
3	Pixel 3	3.97E-10	8.98E-05	94.57
4	Pixel 4	4.17E-10	9.15E-05	96.29
5	Pixel 5	4.32E-10	9.28E-05	97.71
6	Pixel 6	4.42E-10	9.45E-05	99.43
7	Pixel 7	4.52E-10	9.55E-05	100.57
8	Pixel 8	4.62E-10	9.66E-05	101.71
9	Pixel 9	4.72E-10	9.77E-05	102.86
10	Pixel 10	4.87E-10	9.93E-05	104.57
11	Pixel 11	5.02E-10	1.01E-04	106.29
12	Pixel 12	5.17E-10	1.03E-04	108.00
13	Pixel 13	5.32E-10	1.04E-04	109.71
14	Pixel 14	4.37E-10	9.39E-05	98.86
15	Pixel 15	3.92E-10	8.90E-05	93.71
16	Pixel 16	5.37E-10	1.00E-04	105.71
Average		**4.50E-10**	**9.50E-05**	**100.00**
Standard deviation		**5.61E-11**	**5.81E-06**	**6.11**
RSD		**12.47%**	**6.11%**	
Working-pixel yield			**16/16 = 100%**	

Notes: RSD = standard deviation / average × 100%. Normalized photocurrent is calculated relative to the average photocurrent.

References

1 M. Han, J. Sun, M. Peng, N. Han, Z. Chen, D. Liu, Y. Guo, S. Zhao, C. Shan, T. Xu, X. Hao, W. Hu and Z. Yang, *J. Phys. Chem. C*, 2019, **123**, 17566–17573.

2 Z. Gao, H. Zhou, K. Dong, C. Wang, J. Wei, Z. Li, J. Li, Y. Liu, J. Zhao and G. Fang, *Nano-Micro Lett.*, 2022, **14**, 215.

3 T. Liu, J. Wang, Y. Liu, L. Min, L. Wang, Z. Yuan, H. Sun, L. Huang, L. Li and X. Meng, *Adv. Mater.*, 2024, **36**, 2400090.

4 Z. Lv, G. Pan, S. Wang, Y. Xie, H. Tang, D. Wang, H. Gao, Y. Mao and W. Xu, *Adv. Funct. Mater.*, 2026, e75511.

5 X. Ma, Y. Xu, S. Li, T. W. Lo, B. Zhang, A. L. Rogach and D. Lei, *Nano Lett.*, 2021, **21**, 9195–9202.

6 V. Vuong, S. V. N. Pammi, K. S. Pasupuleti, W. Hu, V. D. Tran, J. S. Jung, M. Kim, V. Pecunia and S. G. Yoon, *Adv. Opt. Mater.*, 2021, **9**, 2100192.

7 V.-H. Vuong, S. V. N. Pammi, S. Ippili, V. Jella, T. Nguyen Thi, K. Sairam Pasupuleti, M.-D. Kim, M. Ji Jeong, J.-R. Jeong, H. Sik Chang and S.-G. Yoon, *Chem. Eng. J.*, 2023, **458**, 141473.

8 V. Vuong, S. Ippili, S. V. N. Pammi, J. Bae, T. Yang, M. J. Jeong, H. S. Chang, M. Jeon, J. Choi, M. T. Tran, V. Tran, V. Jella and S. Yoon, *Small Methods*, 2024, **8**, 2400310.

9 A. Waleed, M. M. Tavakoli, L. Gu, S. Hussain, D. Zhang, S. Poddar, Z. Wang, R. Zhang and Z. Fan, *Nano Lett.*, 2017, **17**, 4951–4957.

10 J. Song, L. Xu, J. Li, J. Xue, Y. Dong, X. Li and H. Zeng, *Adv. Mater.*, 2016, **28**, 4861–4869.

11 X. Tang, H. Zhou, X. Pan, R. Liu, D. Wu and H. Wang, *ACS Appl. Mater. Interfaces*, 2020, **12**, 4843–4848.

12 D. Wu, H. Zhou, Z. Song, M. Zheng, R. Liu, X. Pan, H. Wan, J. Zhang, H. Wang, X. Li and H. Zeng, *ACS Nano*, 2020, **14**, 2777–2787.

13 J. Tao, Z. Xiao, J. Wang, C. Li, X. Sun, F. Li, X. Zou, G. Liao and Z. Zou, *J. Alloys Compd.*, 2020, **845**, 155311.

14 C. Perumalveeramalai, J. Zheng, Y. Wang, H. Guo, S. V. N. Pammi, R. Mudike and C. Li, *Chem. Eng. J.*, 2024, **492**, 152213.

15 S. V. N. Pammi, V. Tran, R. Maddaka, J. Eom, J. S. Jung, H. Jeong, M. Kim, V. Pecunia and S. G. Yoon, *Adv. Opt. Mater.*, 2020, **8**, 2000845.